Measurement 149 (2020) 106982

Contents lists available at ScienceDirect

Measurement

journal homepage: www.elsevier.com/locate/measurement

Coupling heterostructure of thickness-controlled nickel oxide nanosheets layer and titanium dioxide nanorod arrays via immersion route for self-powered solid-state ultraviolet photosensor applications

M.M. Yusoff [a,c], M.H. Mamat [a,b,*], M.A.R. Abdullah [a], A.S. Ismail [a], M.F. Malek [a,b], A.S. Zoolfakar [a], S.A.M. Al Junid [a], A.B. Suriani [d], A. Mohamed [d], M.K. Ahmad [e], I.B. Shameem Banu [f], M. Rusop [a,b]

[a] NANO-ElecTronic Centre (NET), Faculty of Electrical Engineering, Universiti Teknologi MARA (UiTM), 40450 Shah Alam, Selangor, Malaysia
[b] NANO-SciTech Centre (NST), Institute of Science (IOS), Universiti Teknologi MARA (UiTM), 40450 Shah Alam, Selangor, Malaysia
[c] Kulliyyah of Engineering, International Islamic University Malaysia (IIUM), 50728 Kuala Lumpur, Malaysia
[d] Nanotechnology Research Centre, Faculty of Science and Mathematics, Universiti Pendidikan Sultan Idris (UPSI), 35900 Tanjung Malim, Perak, Malaysia
[e] Microelectronic and Nanotechnology –Shamsuddin Research Centre (MiNT-SRC), Faculty of Electrical and Electronic Engineering, Universiti Tun Hussein Onn Malaysia (UTHM), 86400 Batu Pahat, Johor, Malaysia
[f] Department of Physics, B.S. Abdur Rahman Crescent Institute of Science & Technology, Vandalur, Chennai 600 048, India

ARTICLE INFO

Article history:
Received 23 April 2018
Received in revised form 21 June 2019
Accepted 23 August 2019
Available online 26 August 2019

Keywords:
Semiconductors
TiO_2 nanorods
NiO nanosheets
Immersion route
Photosensor
Electronic materials

ABSTRACT

A coupling heterostructure consisting of nickel oxide nanosheets (NNS) and titanium dioxide nanorod arrays (TNAs) was fabricated for self-powered solid-state ultraviolet (UV) photosensor applications. By controlling the thickness of the NNS layer by via varying the growth time from 1 to 5 h at a deposition temperature of 90 °C, the coupling NNS/TNAs heterojunction films were formed and their structural, optical, electrical and UV photoresponse properties were investigated. The photocurrent measured from the fabricated self-powered UV photosensor was improved by increasing the thickness of NNS from 140 to 170 nm under UV irradiation (365 nm, 750 μWcm^{-2}) at 0 V bias. A maximum photocurrent density of 0.510 $\mu A{\cdot}cm^{-2}$ was achieved for a sample with a NNS thickness of 170 nm and prepared with a 3 h NNS growth time. Our results showed that the fabricated NNS/TNAs heterojunction has potential applications for self-powered UV photosensors.

1. Introduction

Titanium dioxide (TiO_2) has been widely studied due to its high physical and chemical stability, low cost, abundance and generally non-toxicity [1,2]. Intrinsically, TiO_2 is an n-type semiconductor with a wide band gap of 3.0–3.4 eV, which makes it applicable for the application of a UV photosensor [3,4]. However, the UV photoresponse of TiO_2 is limited by the fast recombination of photogenerated electron-hole pairs [5]. The improvement of charge carrier separation is highly important. It has been suggested that the addition of a dopant or heterogeneous oxide materials on TiO_2 can be used to trap electrons and hinder the recombination of electron-hole pairs [6,7]. The utilization of heterogeneous structures on TiO_2, however, often requires deposition at a high temperature and pressure [8]. This process is costly for large-scale productions. Therefore, facile and cheaper alternatives need to be identified for the enhancement of the UV photoresponse of TiO_2 through heterogeneous structure deposition.

Several lines of evidence suggest that a hybrid structure of TiO_2 and semiconductors such as ZnO, NiO, SnO_2, CdS, Co_3O_4 and Cu_2O could effectively hinder the recombination of photogenerated charge carriers. These structures would impact the transportation of excitonic electrons and holes into the heterojunction and extend their lifetime to improve the photoresponse activity [9–12]. Among these hybrid nanostructures, a considerable amount of literature has been dedicated to the TiO_2/NiO heterojunction. Recent developments involved the high hole concentration and mobility of the p-type NiO [13,14]. The non-stoichiometric defect states in the NiO lattice form Ni^{2+} vacancies and generate holes in the NiO [15]. Calculations of NiO also suggested that the charge is more delocalized, with Ni ions situated around the vacancy and trapped in it, or delocalized over other Ni ions [16]. Therefore, the Ni^{2+} vacancies form delocalized holes, which produce the p-type conductivity in NiO.

NiO is also a widely investigated material due to its large modulation range, natural abundance and low material cost [17,18].

* Corresponding author.
E-mail address: mhmamat@uitm.edu.my (M.H. Mamat).

https://doi.org/10.1016/j.measurement.2019.106982
0263-2241/

Previous examples of research into TiO_2/NiO composites comprised of diverse nanostructures include deposition or growth of NiO on TiO_2 surfaces and mixing of both TiO_2 and NiO components [19,20]. There is also a few published studies describing the role of NiO in TiO_2/NiO composites to decrease the recombination of photo-generated electron and hole pairs using a heterojunction in the working electrode [19,21]. However, such studies remain narrow in focus, dealing only with the efficiency and output of the fabricated nanomaterials. The synthesis and deposition often require complicated processes and conditions. In addition, simple synthesis and deposition methods for proficient photoresponse activity of the heterojunction with a tunable morphology and crystallinity of NiO for desirable UV absorption characteristic are still lacking. To optimize the UV photoresponse performance of TiO_2/NiO composites, a tunable morphology, crystallinity and good contact between TiO_2 and NiO must be determined for enhancing the total photocurrent gain. In addition, a high effective surface area needs to be produced to improve the performance of the UV photosensor.

In recent years, there has been renewed interest in one-dimensional (1D) TiO_2 nanorod arrays (TNAs) in an extensive range of fields. They have been proposed for UV photosensor applications, particularly due to their large surface-to-volume ratio, high electron mobility and efficient light scattering ability within the nanorod structure [22–24]. It was previously established by the authors that TNAs may show excellent UV photoresponse performance in an electrolyte solution under UV irradiation due to their structural, optical and electrical properties [25]. TNAs were synthesized and deposited on a FTO-coated glass substrate through an improved one-step aqueous chemical route using a simple modified Schott bottle in an electric oven with a low temperature and low deposition time. It is postulated that advancements of TNAs, with other solid-state metal oxides, could lead to the formation of nanocomposite materials with tunable nanostructures and compositions for enhancing the UV photoresponse performance of a UV photosensor.

In this paper, the effect of NNS thickness on the properties of the synthesized NNS/TNAs heterojunction was investigated because the synthesis of NNS/TNAs offers a method to enhance the UV photoresponse properties of the nanostructures. In addition, the fabrication of a NNS/TNAs heterojunction-based UV photosensor is rarely reported in the literature. Based on a thorough literature review, it was found that the deposition of NNS on developed TNAs using an immersion method based on a facile Schott bottle has not yet been investigated. Thus, the effect of various NNS growth parameters on the fabrication of heterojunction-based UV photosensors, and subsequent analysis of the electron transport properties, have not been thoroughly examined. Therefore, we believe that this work has novelty in terms of fabrication process and the application of NNS/TNAs heterojunction as a UV sensor. Particularly in this study, the influence of NNS thicknesses on structural, optical and electrical properties of the synthesized and deposited NNS were examined in advance for the application of a heterojunction-based self-powered UV photosensor. This preparation method of NNS/TNAs nanocomposites materials is amenable to fast, effective and large-scale production, and shows potential application as an effective UV photosensor.

2. Experimental details

2.1. Synthesis of TNAs

TNAs were deposited using an aqueous chemical method as described in previous work [26]. The first step in this process was to clean the fluorine tin oxide (FTO) coated glass substrate with acetone, ethanol and deionized (DI) water in an ultrasonic bath. To begin the aqueous chemical process, hydrochloric acid (37%, Merck) and DI water in a 1:1 vol ratio were added in a Schott bottle. After the chemical was stirred for 10 min, 0.07 M titanium (iv) butoxide (97%, Sigma-Aldrich) was gently added into the chemical and stirred for another 30 min. After that, a cleaned FTO-coated glass substrate was immersed in the prepared solution with the conductive side facing upward. The bottle was then tightly sealed with a bottle cap and heated at 120 °C in an electric oven for 3 h. The deposited TNAs were rinsed with DI water and dried at room temperature before annealing in a furnace at 450 °C for 1 h to improve crystallinity.

2.2. Synthesis of NNS

A mixture of sol–gel containing DI water, 0.1 M nickel nitrate hexahydrate ($Ni(NO_3)_2{\cdot}6H_2O$ 98%, Sigma-Aldrich) and 0.1 M hexamethylenetetramine ($C_6H_{12}N_4$, Sigma–Aldrich) was prepared in a Schott bottle and stirred for 2 h, as illustrated in Fig. 1. The deposited TNAs on a FTO-coated glass substrate were immersed in the prepared sol–gel with the active side facing upward. The bottle was then tightly sealed with a bottle cap and heated to 90 °C in a water bath to deposit NNS on the deposited TNAs. Five samples were prepared at different thicknesses based on various deposition times of 1, 2, 3, 4 and 5 h, and designated as TN_1, TN_2, TN_3, TN_4 and TN_5, respectively. The samples were cleaned with DI water and dried at room temperature before annealing in a furnace at 450 °C for 2 h to improve crystallinity.

2.3. Deposition of counter electrode

A 90-nm thick platinum (Pt) layer was deposited on the top of the NNS layer for TN_1-TN_5 samples using a thermal evaporator (ULVAC). This layer acted a counter electrode for the fabricated heterojunction-based UV photosensor. The Pt electrode was also deposited on the bare TNAs as a reference. The effective area was approximately 1.0 cm^2 at the center of the photosensor device for the detection of UV irradiation.

2.4. Characterization

The characterization of the samples was performed via field-emission scanning electron microscopy (FESEM, JEOL JSM-7600F), X-ray diffraction (XRD, Shimadzu XRD-6000, Cu Kα radiation, wavelength 1.54 Å) and UV–Vis-NIR spectrophotometry (Cary 5000) for morphology and cross-section images, crystallinity and optical properties, respectively. The current–voltage (I-V) characteristics of the deposited samples were characterized via direct current (DC) two-probing system semiconductor device analyzer (Keysight B1500A). The photocurrent properties of the fabricated sample were measured using a UV photocurrent measurement system (Keithley 2400) under a UV lamp (365 nm, 750 μWcm^{-2}).

3. Results and discussion

3.1. Surface morphology and Cross-Sectional images

Fig. 2(a)–(f) show the surface morphology images for synthesized TNAs and NNS/TNAs heterojunctions at different NNS thicknesses or deposition times (TN_1-TN_5). The formation of a thin layer of two-dimensional (2D) NNS can be clearly observed in all TN_1-TN_5 samples. The growth of NNS across the TNAs surfaces was also uniform. With the increase of the deposition time, the TNAs structure was gradually concealed, which indicates that the density of NNS layer increased. A longer deposition time also

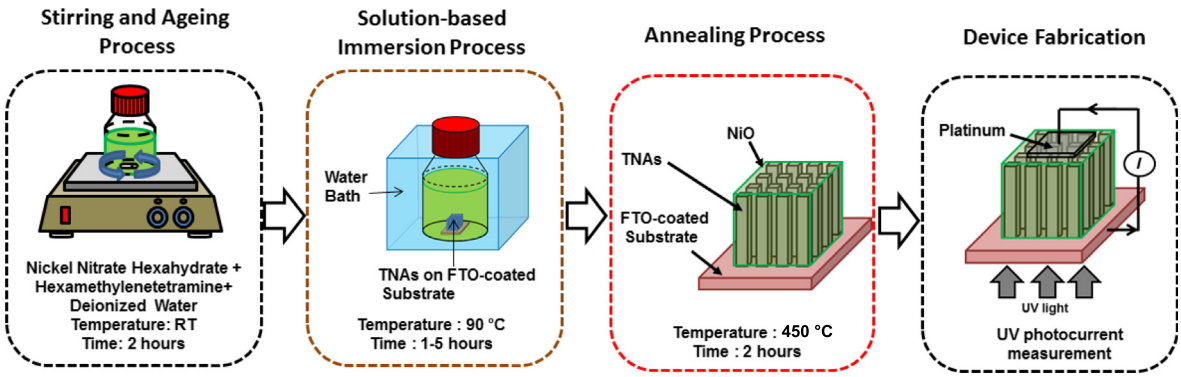

Fig. 1. Schematic of NNS/TNAs heterojunction preparation procedure.

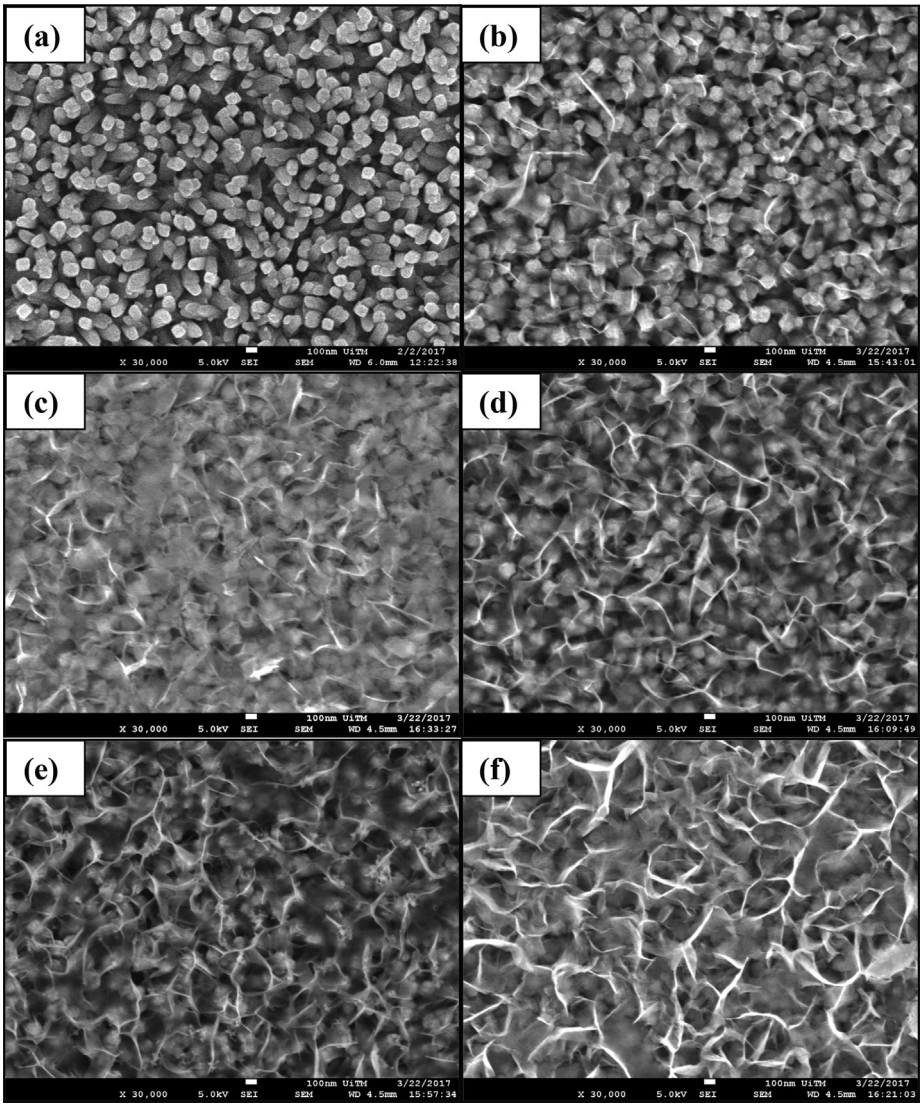

Fig. 2. FESEM surface morphology of (a) TNAs, (b) TN_1, (c) TN_2, (d) TN_3, (e) TN_4 and (f) TN_5 samples.

allowed Ni ions in solution to better infiltrate the TNAs layer, enabling the formation of a better interpenetrated network of the NNS/TNAs heterojunction.

Fig. 3(a)–(f) display cross-sectional FESEM images of deposited TNAs and NNS/TNAs heterojunctions at various NNS thicknesses or deposition times. The thickness or length of the TNAs used in this study was approximately 410 nm, as shown in the cross-sectional FESEM image in Fig. 3(a). The aligned TNAs on a FTO-coated glass substrate were expected to promote electron transportation due to the direct pathway of the nanorod structure. The cross-sectional images show a significant increase of NNS layer on the surface of TNAs with increasing deposition time, which agrees with previous

surface morphology results. Interestingly, the formation of NNS grew in between the nanorod structure and on top of TNAs. The overall thickness of the deposited films was approximately 550, 570, 580, 600 and 605 nm for TN_1, TN_2, TN_3, TN_4 and TN_5 samples, respectively. A significant increase in thickness compared to bare TNAs can be observed with the deposition of the NNS. From this result, it was estimated that an average thickness of the deposited NNS layer was approximately 140, 160, 170, 190 and 195 nm for TN_1, TN_2, TN_3, TN_4 and TN_5 samples, respectively.

3.2. X-Ray diffraction analysis

Fig. 4 shows the XRD result of the deposited TNAs and NNS/TNAs heterojunctions at various NNS thicknesses of TN_1-TN_5 samples. After the deposition of NNS, all diffraction peaks of rutile TiO_2 (JCPDS No. 01–072-1148) were still detected, suggesting that there was no TiO_2 phase change after depositing NiO. The existing peaks of rutile TiO_2 also suggest that a thin film of NiO was deposited on the TNAs, in agreement with the FESEM results. The diffraction peaks detected at 2θ degrees of 37.1°, 43.3° and 62.9° can be readily indexed as (1 1 1), (2 0 0) and (2 2 0) planes, respectively, for cubic NiO (JCPDS No. 47–1049). However, it was hard to obtain high-intensity XRD peaks for NiO due to the thinness and porous structure of the NiO layer, which is in line with a previous study [27]. The average crystallite size, *D*, of the TNAs and NNS were calculated using Scherrer's formula in Eq. (1):

$$D = \frac{0.94\lambda}{\beta \cos\theta} \tag{1}$$

where λ is the X-ray wavelength (1.54 Å), β is the full width at half maximum (FWHM) of the represented plane and θ is the peak position of the plane. The XRD pattern for the (0 0 2) plane was utilized to evaluate the crystallite size of the TNAs, which apparently has a significant effect on the improvement of charge transportation [28].

The crystallite size of the TNAs was found to be 23.1 nm. Meanwhile, the most intense peak for the (1 1 1) plane was used to calculate the crystallite size of the NNS, and the calculated values are presented in Table 1. The average crystallite sizes of the NNS were in the range of 25.6–30.8 nm for TN_1–TN_5 samples. These results show that the crystallite size increased with increasing deposition time or NNS thickness. The results also indicate the growth mechanisms, which are the nucleation and crystallization that are convoluted in an aqueous chemical growth. Nuclei formed per unit

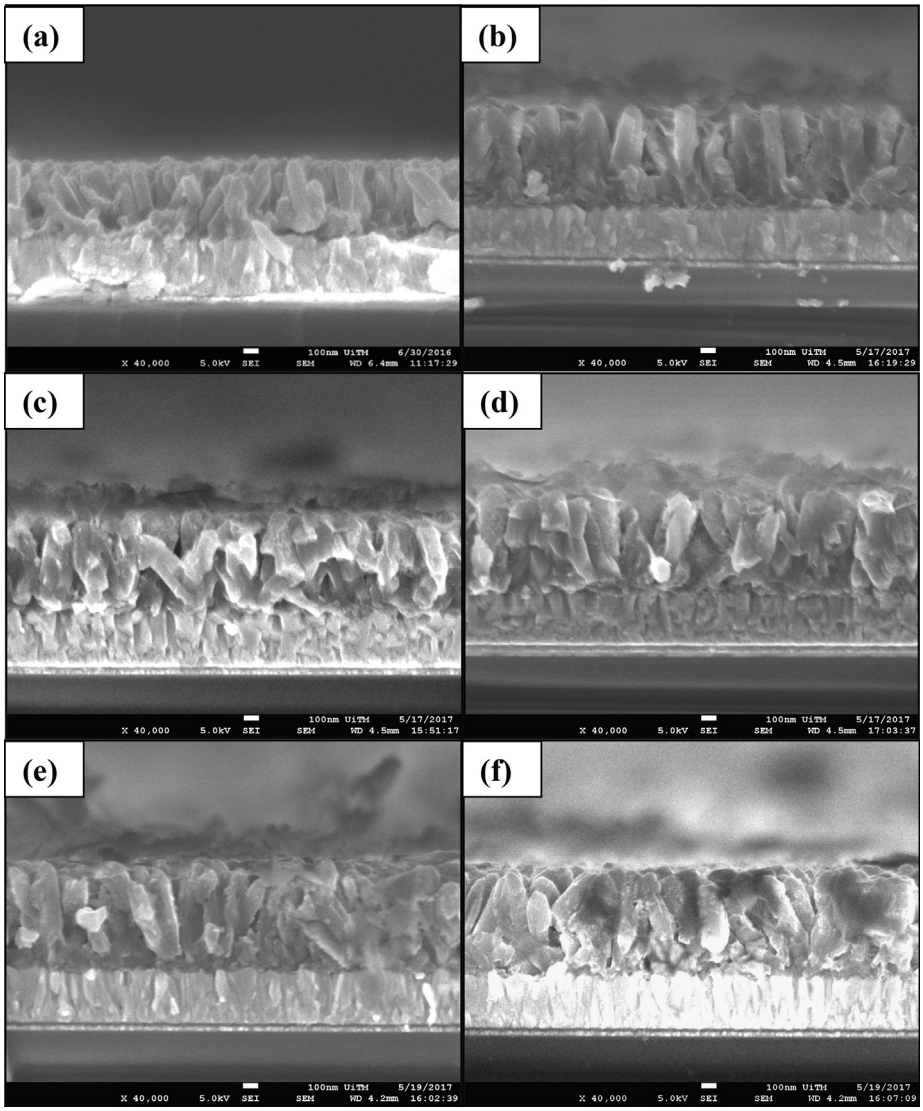

Fig. 3. Cross-section images of (a) TNAs, (b) TN_1, (c) TN_2, (d) TN_3, (d) TN_4 and (e) TN_5 samples.

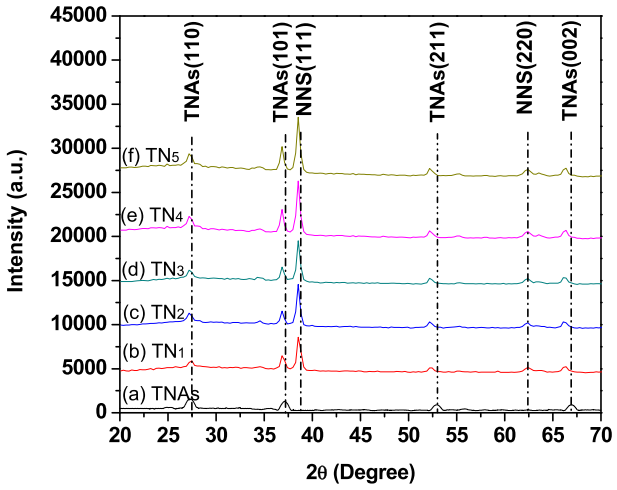

Fig. 4. XRD patterns for TNAs and NNS/TNAs heterojunction films.

area aided the growth of the crystals, which led to the increase in the crystallite size [29,30].

The XRD data of synthesized NNS at various thicknesses was utilized to calculate the lattice parameter of *a* based on the (1 1 1) plane of the XRD patterns, according to the following Eq. (2) [31]:

$$\frac{1}{d^2} = \frac{h^2 + k^2 + l^2}{a^2} \tag{2}$$

where *h, k, l* are the miller indices, and *d* is the interplanar spacing, which is based on 2θ from Bragg's Law in Eq. (3):

$$d = \frac{\lambda}{2\sin\theta} \tag{3}$$

The determined lattice parameters in Table 1 reveal that there was a steady increase from 4.204 Å to 4.213 Å for the NNS lattice parameter, *a*, when the NNS deposition time or thickness increased. The results indicate that a positive correlation was found between NNS thickness and the lattice parameter, *a*. The strain along the NNS *a*-axis, ζ_a, was calculated using the following formula in Eq. (4) [32]:

$$\zeta_a(\%) = \frac{a - a_o}{a_o} \times 100 \tag{4}$$

where *a* is the lattice parameter of the strained NNS obtained from the XRD data and a_o is the standard value of the unstrained NiO, whose value is 4.177 Å. A positive value indicates a tensile strain, while a negative sign indicates a compressive one. The strain estimation in Table 1 shows that the strain in all deposited samples was tensile. The strain rose from 0.656% to 0.850% for TN_1 to TN_5 samples, demonstrating the construction of a more strained structure with increasing NNS thickness. Hence, a more relaxed structure could be obtained at a lower NNS thickness. The strain values also indicate that the lattice parameter, *a*, of the NNS was elongated along the unit cell of the *a*-axis. The strain therefore contributed to the formation of a distorted unit cell structure, compared to bulk NiO.

3.3. Optical properties

Fig. 5 presents the UV–Vis transmittance spectra of TNAs and NNS/TNAs heterojunctions at room temperature for TN_1-TN_5 samples in the wavelength range approximately from 320 to 1200 nm. The rutile phase of the TNAs and NNS/TNAs samples transmitted visible light (>400 nm) and absorbed the incident light in the UV region (<400 nm) through the sharp edges. The thickness of NNS layer had great influence on the transmittance spectra. The average transmittance in the visible region (400–800 nm) decreased with increasing NNS deposition time, as shown in Fig. 5. The average transmittance of the TNAs in the visible region was estimated to be 55%. However, the transmittance in the visible region slightly decreased after the deposition of NNS on the top of TNAs, with the average transmittances of 51, 42, 40, 38 and 35%, for TN_1, TN_2, TN_3, TN_4 and TN_5 samples, respectively. The transmittance reached the lowest at the highest deposition time due to the increases in thickness of the NNS layer. The increment of these factors may have increased the optical scattering in between the grain boundaries, which reduced the transmittance of the deposited films.

The result based on the UV–Vis spectra was used to calculate the absorption coefficient using Lambert's Law based on the relation below in Eq. (5):

$$\alpha = \frac{1}{t}\ln\left(\frac{1}{T}\right) \tag{5}$$

where *t* is the thickness of the film and *T* is the transmittance of the film. The absorption coefficients of TNAs and NNS/TNAs heterojunctions produced at various NNS thicknesses are presented in Fig. 6. The data reveals that there was a steady decrease in the number of absorption coefficients with increasing NNS thickness below the UV region. In addition, sharp edges can also be observed below the UV region (<380 nm) for all samples due to the photon, which has energy above the band gap of TiO_2 and excited an electron into the conduction band from the valence band. The decrease of the UV absorption coefficient with increasing NNS deposition time might be due to the defect formation during the NNS growth.

The optical band gap energy, E_g, of the deposited samples were also determined using the Tauc plot in the UV and visible range according to the following relation in Eq. (6) [33]:

$$(\alpha h\nu)^2 = A(h\nu - E_g) \tag{6}$$

where α is the absorption coefficient, $h\nu$ is the photon energy, E_g is the optical band gap and *A* is an absorption constant. The optical band gap energy, E_g, was determined by the extrapolation of the linear portion of the plotted graph presented in Fig. 7 for the $(\alpha h\nu)^2$ versus $h\nu$ curve for the deposited TNAs and TN_1-TN_5 samples. The

Table 1
Average diameter and thickness of TNAs, average thickness of NNS/TNAs, average thickness of NNS, lattice parameter, strain, crystallite size and optical bandgap of NNS/TNAs prepared at various deposition time.

Samples	Average Diameter/Thickness of TNAs (nm)	Average Thickness of NNS/TNAs (nm)	Average Thickness of NNS (nm)	Lattice Parameter of *a* (Å)	Strain of *a*-axis (%)	Crystallite Size (nm)	Optical Bandgap Energy (eV)
TN_1	75/410	550	140	4.204	0.656	25.6	3.41
TN_2	75/410	570	160	4.209	0.766	26.6	3.40
TN_3	75/410	580	170	4.210	0.798	27.0	3.39
TN_4	75/410	600	190	4.212	0.829	28.6	3.35
TN_5	75/410	605	195	4.213	0.850	30.8	3.34

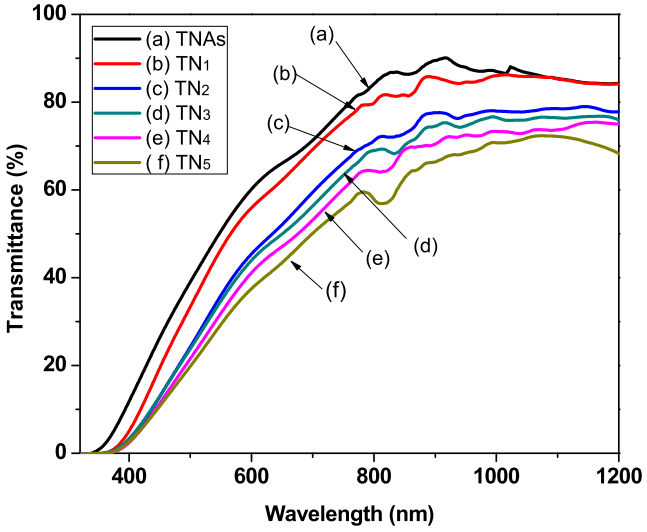

Fig. 5. Transmittance spectra of TNAs and NNS/TNAs heterojunction for TN_1-TN_5 samples.

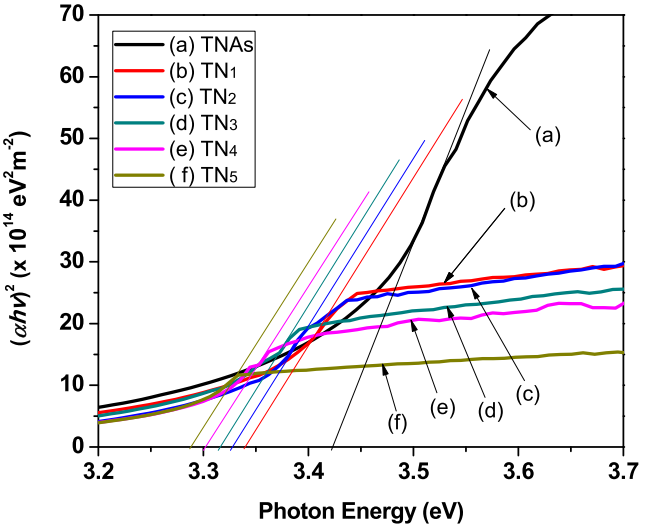

Fig. 7. Tauc plot of TNAs and NNS/TNAs heterojunction for TN_1-TN_5 samples.

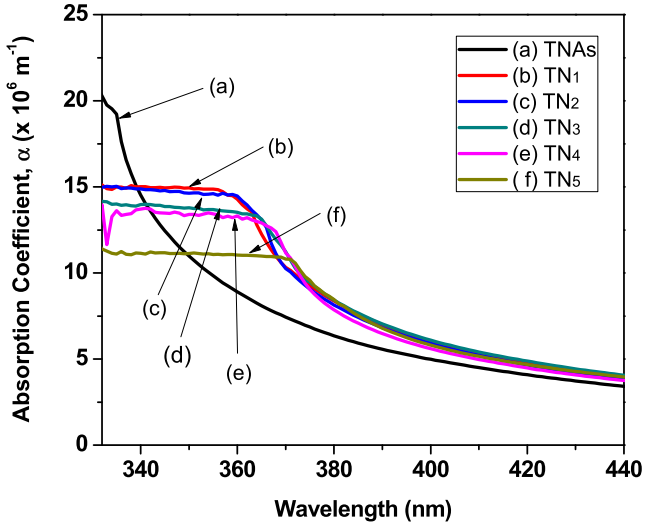

Fig. 6. Absorption coefficient, α, of TNAs and NNS/TNAs heterojunction films.

optical bandgap values at various NNS thicknesses are presented in Table 1. The transition results exhibit a fine linear curve in the band edge region, inferring that the transition of deposited rutile phase TNAs is direct in nature [34,35]. For all the deposited samples, the band gap reduced from 3.41 eV to 3.34 eV with increasing NNS thickness layer based on the deposition time. This result appears consistent with other reports [27,36] that explained the synergy between the heterojunction layer and both metal oxides. In addition, a small band gap can enhance the transfer of photogenerated charge carriers and consequently improve the electrochromism of the thin film [27]. The conclusion that emerged from these studies is that a light spectrum with a wavelength shorter than 380 nm can be absorbed by the deposited NNS/TNAs heterojunction samples and contribute to the photoresponse activity of NNS/TNAs layer.

3.4. Current-Voltage characteristics

Fig. 8(a) shows the *I–V* characteristic of the TNAs and NNS/TNA heterojunction films. The *I–V* plot of the TNAs shows an Ohmic characteristic for the Pt and FTO electrodes, as shown by a linear *I-V* curve in the magnified images in Fig. 8(b). On the other hand, the *I–V* plots of NNS/TNAs heterojunctions in Fig. 8(a) obviously show a nonlinear and asymmetric *I–V* curve. This rectifying characteristic is likely to be related to the formation of a p–n heterojunction between the p-type NNS and the n-type TNAs. From the data in Fig. 8, it is apparent that the threshold voltage at the forward bias to overcome the potential barrier of TN_1-TN_5 samples increased with increasing thickness of NNS on the TNAs. This result may be explained by the fact that the resistance of the deposited layer increased with increasing NNS thickness. The formation of the p-n junction indicates the existence of a depletion layer or space charge region at the transition between p-type NNS and n-type TNAs. The depletion layer is the most subtle part of the p-n junction type sensor, and a small adjustment in the concentration of free electrons and holes significantly changes the overall resistivity [37]. Thus, while the electrons from the n-type TNAs remain constant regardless of increasing holes from the p-type NNS, the net resistance and electric field inside the cell determines the overall threshold voltage in the system.

3.5. Ultraviolet sensing performance

The performance of fabricated NNS/TNAs heterojunction-based self-powered UV photosensor was measured through the generated photocurrent under "on" and "off" states during repeated switching cycles with 365 nm UV irradiation at 0 V bias, as shown in Fig. 9. One interesting finding is that the fabricated UV photosensor based on NNS/TNAs heterojunctions can function independently, without any external bias voltage. It can be seen from the graph that all samples exhibited a rapid change of the photocurrent during the "on" and "off" states. The stability and rapid change of the photogenerated current observed in all samples also suggested that the fabricated UV photosensor reacted to a rapid change of the optical signal. This condition is due to the swift transfer of photogenerated charge carriers to the electrodes because of the built-in potential at the p-n junction. This generated photocurrent may be explained by the UV irradiation, which provides energy higher than the band gap energy level of the deposited TNAs and is able to excite the electrons from the valence band to conducting band and leave holes in the TNAs valence band, as illustrated in Fig. 10(a).

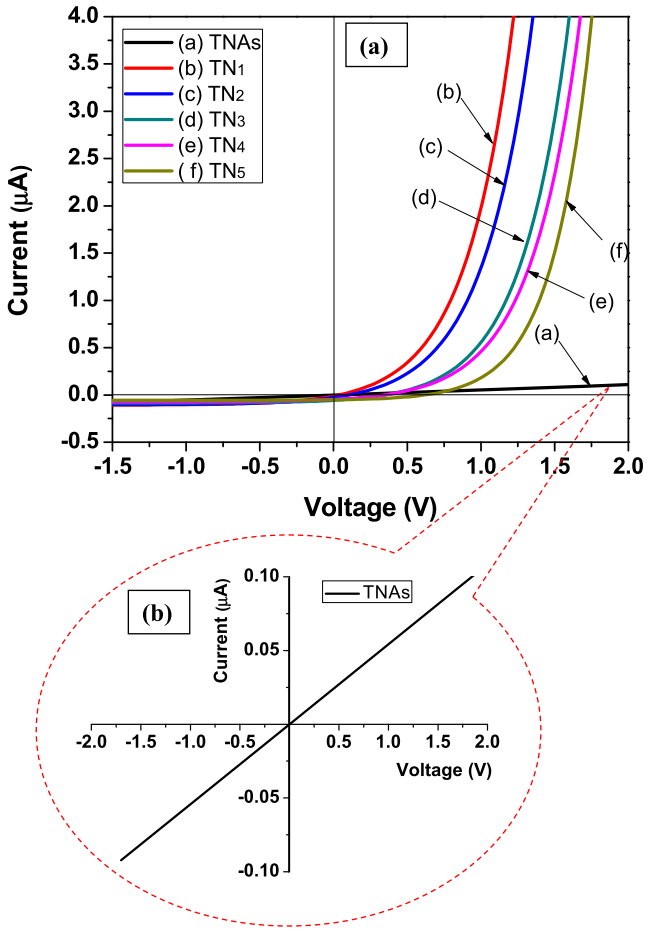

Fig. 8. (a) *I–V* curves of the TNAs and NNS/TNAs heterojunction. (b) Magnified *I-V* plot of TNAs showing the Ohmic characteristic of TNAs with Pt and FTO electrodes.

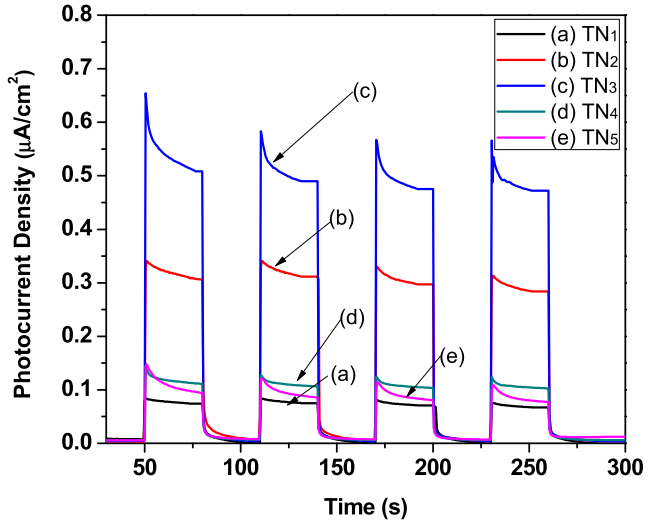

Fig. 9. Photocurrent response under UV irradiation (365 nm, 750 μW/cm^2) of fabricated NNS/TNAs heterojunction-based UV photosensors at 0 V bias.

In general, the majority charge carriers for n-type materials is electrons and is holes for p-type materials. Hence in this study, TiO_2 primarily exhibits n-type conduction by electrons and NiO shows p-type conduction by holes. Initially, when a p–n heterojunction is formed in an opened loop circuit, a local electric field is built at the interface between the p-type and the n-type materials, thereby allowing electrons and holes to diffuse into the opposite directions and create the space charge region. This region is known as a depletion layer with a potential barrier where electrons are depleted [38]. The donor and acceptor concentrations are equal in this region and the created electric field is sufficient to oppose the continued exchange of charge carriers. In addition, when the grown TNAs are exposed to air, a surface charge region will develop on the surface of TNAs from to the adsorption of oxygen molecules, which increases the resistance of the detecting system. The construction of a p-n junction with a surface charge region will further increase the resistance of the sensing device [39]. In a closed loop circuit, the generation of dark current in the "off" state, as shown in Fig. 9, could be attributed to the migration of excess electrons from the semiconductor to a higher conductivity material. This process would involve passing through the external circuit and recombining with the holes in the opposite direction. In addition, the metal has a higher work function and Fermi level than the semiconductor [40,41].

During the "on" state under UV irradiation, the photogenerated charge carriers increase the excess electrons in the deposited TNAs to flow toward the FTO-coated glass substrate through the nanorods and become part of the external circuit, which then flow toward the Pt electrode and recombine with the holes in the NNS region, as shown in Fig. 10(a). Meanwhile, the photogenerated holes in the TNAs region diffuse toward the opposite direction in the depletion region to replace the recombined holes in the NNS region and sustain the equilibrium of the donor and acceptor concentrations in the space charge region. In contrast, the excited electrons and holes under UV irradiation in a bare TNAs migrate randomly to the surface or otherwise recombine. Most of the photogenerated electron-hole pairs in this condition are recombined, resulting in very poor quantum efficiency in the UV photoresponse process [42]. The formation of a built-in potential difference at the p-n junction of the NNS/TNAs heterojunction moves the electron and hole in opposite directions to minimize recombination and increase quantum yield. This built-in potential difference strengthens the electron–hole separation, causing a better photoresponse performance. Hence, the excess photo-generated electrons drifted to the conductive side at the back contact of FTO coated glass substrate through the nanorods [6], under the influence of the built-in potential difference. This difference constituted the photocurrent in the external circuit, while the photogenerated holes are conceptually diffused towards the NNS/platinum interface. Thus far, several studies have reported that p-type NiO materials act as hole traps and collectors [43,44]. Hence, the photo-generated electrons form an external current and move towards the platinum electrode to recover the photo-generated holes and complete the closed-loop circuit.

The performance of the fabricated UV photosensor was therefore mainly based on the mobility of photogenerated electron-hole pairs. The generated photocurrent reduced the total resistance during the "on" state, and instantaneously returned to initial value during the "off" state [45,46]. The generated photocurrent densities of the fabricated UV photosensor from NNS/TNAs p-n heterojunctions are summarized in Table 2. The UV photosensor fabricated from TN_1 sample showed photocurrent density of 0.095 μA/cm^2. The growth in NNS thickness increased the generated photocurrent density to 0.332 and 0.510 μA/cm^2 for TN_2 and TN_3 samples, respectively. The increase in photocurrent density values could be attributed to the increase of the inner built-in potential difference with increasing NNS layer thickness, which offered a driving mechanism for the initial separation of charge carriers and the mobility of the excess photocurrent.

When the NNS thickness was further increased for TN_4 and TN_5 samples, the measured photocurrent density started to decrease to

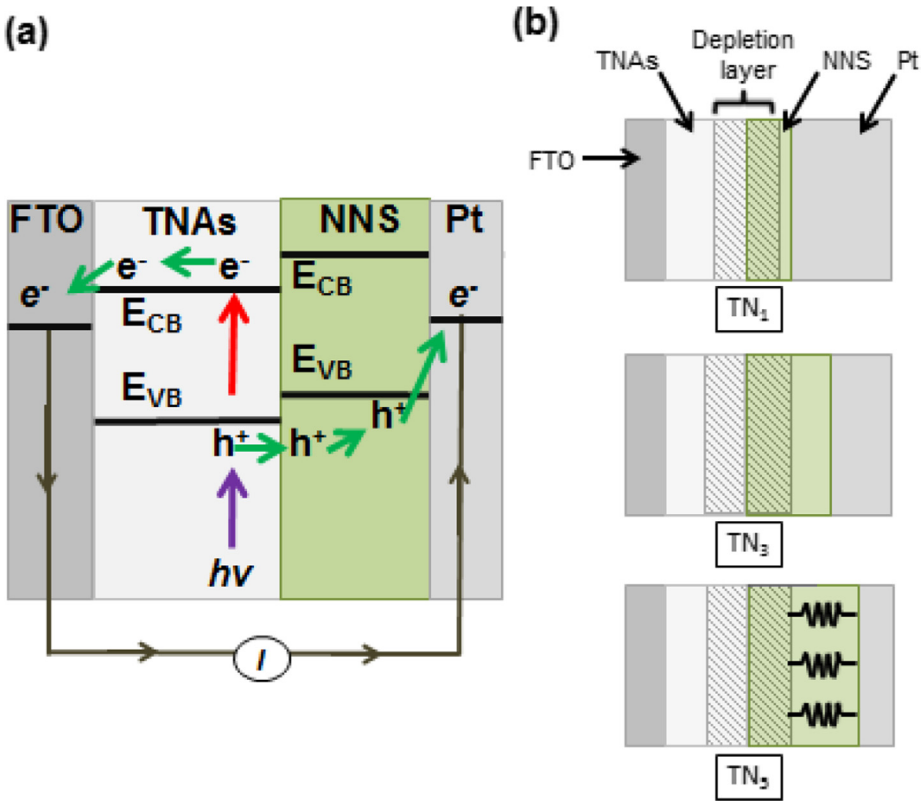

Fig. 10. (a) The energy band diagram of NNS/TNAs heterojunction device under UV irradiation. (b) Diagram of different NNS thicknesses of TN1, TN3 and TN5 samples, respectively (The depletion layers are represented by slash lines).

0.107 μA/cm^2 and further decreased to 0.086 μA/cm^2, respectively. The results of the measured photocurrent density suggest that the performance of the fabricated photosensor was not improved as expected with increasing NNS layer thickness. This result may be explained by the potential mechanism, illustrated in Fig. 10(b). The depletion layer of the fabricated UV photosensor from NNS/TNAs p-n heterojunctions with thinner a NNS layer (sample TN_1) was smaller than for the TN_3 sample. Therefore, there were inadequate numbers of interfacial defects and generated charge carriers, which led to the lower generation of photocurrent for the thinner samples. Although the thicker NNS layer for the TN_5 sample had adequate numbers of generated charge carriers due to sufficient formation of the depletion layer, the increasing series resistance from the thicker NNS film decreased the generation of photocurrent. These results are in agreement with previous research, indicating that the increase in the series resistance implies a suppression of the mobility of charge carriers due to the longer pathway, which possibly leads to the recombination of generated electron-hole pairs [47].

The generated photocurrent based on the photoconductivity effect of rutile TNAs depends on a light-trapping and hole-trapping mechanism, in addition to the presence of chemisorbed oxygen molecules [48,49] on the surface of the TNAs. During the initial state without any irradiation, a high-resistance carrier-depletion region is formed at the NNS/TNAs interface due to the existence of free electrons in the n-type TiO_2 material captured by the absorbed oxygen molecules. The oxygen molecules from the environment tend to be adsorbed on the TNAs surface by the capture of a free electron to form adsorbed oxygen ions, as shown by following reaction in Eq. (7):

$$O_2 + e^- \rightarrow O_2^-. \quad (7)$$

Thus, a depletion region near the surface of the TNAs is formed. Upon illumination by UV light on the developed photosensor with an energy exceeding the energy gap of the synthesized material, the electron-hole pairs are generated. The oxygen is consequently desorbed from the surface of this region. The photogenerated holes

Table 2
Photocurrent density, dark current density, responsivity, sensitivity, rise time and fall time of NNS/TNAs heterojunction-based UV photosensor prepared at different deposition time of NNS. The performances of ZnO-based UV sensors are also shown as comparison.

Samples	Photocurrent Density, J_{ph} (μA·cm^{-2})	Dark Current Density, J_{dark} (μA·cm^{-2})	Responsivity (mA/W)	Sensitivity	Rise Time (sec)	Fall Time (sec)
TN_1	0.095	0.008	0.12	11.9	0.05	0.70
TN_2	0.332	0.003	0.44	110.7	0.02	0.20
TN_3	0.510	0.004	0.68	127.5	0.01	0.13
TN_4	0.107	0.005	0.14	21.4	0.05	0.62
TN_5	0.086	0.006	0.11	14.3	0.06	0.77
V-doped ZnO [53]	–	–	1.1×10^{-3}	0.5	150	400
Fe-doped ZnO [54]	–	–	2.73	11.73	–	–

move towards the surface, due to the built-in electric field, to react with adsorbed oxygen ions and produce oxygen molecules. This reaction can be described as follows in Eq. (8):

$$O_2^- + h^+ \rightarrow O_2. \quad (8)$$

This reaction leaves behind a photogenerated electron, which increases the photocurrent density of the devices. The separation of electrons and holes through the built in electric field of the p-n heterojunction also reduces the recombination rate of photogenerated carriers and increases the carrier lifetime. As a result, the photocurrent gain of the p-n heterostructures is increased. The light-trapping and hole-trapping mechanisms are more related to the active surface area to determine the performance of the developed UV photosensor. The increase of the high-resistance carrier-depletion region with increasing thickness layer of NNS contributes to possible recombination and poor generation of photocurrent, as seen in TN_4 and TN_5 samples. The hole-trapping mechanism of the absorbed and desorbed oxygen is also understood to determine the response time of the developed photosensor and become dominant when the materials reach the nanoscale [50]. A possible explanation for this might be that the diffusion of electrons in TNAs is superior to the diffusion of holes in NNS. The diffusion of photo-generated charge carriers is limited by the transportation between the boundaries of the nanostructures and high-resistance carrier-depletion region, which could hinder the moving pathway, and thus increase the possibility of electron recombination, particularly on the thicker structure. Strong evidence of these explanations was found when the TN_3 sample showed optimum photocurrent density (0.510 μA/cm^2), compared to the other samples. This was likely due to the optimum NNS layer thickness for the deposited TNAs layer.

Fig. 11 shows the responsivity and sensitivity of the fabricated NNS/TNAs heterojunction-based self-powered UV photosensor. The responsivity, R, of the sensors was estimated using the following Eq. (9) [51]:

$$R = \frac{J_{ph} - J_{dark}}{P_{op}} \quad (9)$$

where J_{ph} is the photocurrent density, J_{dark} is the dark current density and P_{op} is the optical power density of the UV source (750 μW/cm^2). Note that an effective surface area for the coupling of the NNS/TNAs heterojunction, which was exposed to UV irradiation, is 1 cm^2. The dark current densities for TN_1, TN_2, TN_3, TN_4 and TN_5 were 0.008, 0.003, 0.004, 0.005 and 0.006 μA/cm^2, respectively. From this calculation, the responsivity of the sensors composed of TN_1, TN_2, TN_3, TN_4 and TN_5 was 0.12, 0.44, 0.68, 0.14 and 0.11 mA/W, respectively. This result shows that the sensor composed of TN_3 had a higher responsivity than the other samples.

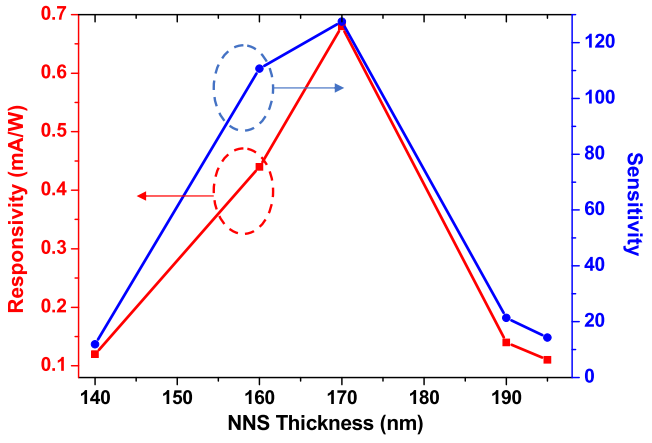

Fig. 11. The responsivity and sensitivity of NNS/TNAs heterojunction-based device at different NNS thicknesses.

The sensitivity of the UV photosensors, which is defined as the photocurrent-to-dark-current ratio, was calculated for all the devices through the measured photocurrent and dark current density under an "on" and "off" states during repeated switching cycles with 365 nm UV irradiation at 0 V bias within a certain time interval. The sensitivity was calculated using the following Eq. (10) [52]:

$$S = \frac{J_{ph}}{J_{dark}} \quad (10)$$

The sensitivity of the sensors composed of TN_1, TN_2, TN_3, TN_4 and TN_5 was 11.9, 110.7, 127.5, 21.4 and 14.3, respectively. The results indicate that the self-powered UV photosensor based on the TN_3 sample had the highest sensitivity. This sensitivity value is higher than the values reported for ZnO-based devices in Refs. [53,54], which can be referred in Table 2. As shown in Table 2, the sensitivity values were highly dependent on the photocurrent density, due to low dark current density, as the measurement was performed at 0 V bias. Based on these results, the responsivity and sensitivity values for the TN_3 sample were the highest, probably due to the optimized NNS thickness that enabled generation of carriers at the optimum level under UV illumination.

Further investigation was done on the performance of fabricated UV photosensors from NNS/TNAs p-n heterojunctions using the recorded photocurrent density data on the rise and fall times of the device. To calculate the speed of the photoresponse of the fabricated device, the current density – time switching curve (Fig. 9) measured at 0 V bias, was analyzed at the rising and falling edges. The rise time is the required time for current density to increase from 10% to 90% of its optimum saturation value, while the fall time is the required time for current density to decrease from 90% to 10% of its minimum saturation value. As shown in Fig. 9, the response time for the photocurrent density was clearly less than 0.1 sec and the J_{dark} was too small and determined to be negligible for all samples. However, the J_{ph} was instantly generated once the UV light was turned on. The fall times were determined to be less than 1.0 sec as illustrated in Table 2, indicating that the fabricated UV photosensor can be proposed for high speed sensing devices. In addition, the photocurrent decay happened upon the "on" state of UV light in all samples. At the start of "on" state, an intense spike was detected and steadily decreased until it reached a saturated value of J_{ph}. This phenomenon could be due to the substantial generation of charge carriers caused by the accumulation of electrons in the bulk, or holes on the surface, which immediately recombined after generation [55]. The result is also likely related to the deficiency in electron transportation in the fabricated device. However, the photocurrent decay was insignificant because the difference between the maximum spike and the stable J_{ph} values was comparatively higher than the J_{dark} value during the "off" state.

4. Conclusion

In summary, NNS/TNAs heterojunctions were successfully deposited on FTO-coated glass substrates using a facile immersion route in a clamped Schott bottle. Different NNS thicknesses were produced by varying the deposition time. The FESEM images revealed that the thickness of the NNS layer increased with increasing deposition time. The XRD patterns showed that the samples consisted of crystalline TNAs and NNS. The fabricated samples exhibited excellent stability and a rapid change of the photocurrent density, and rose and decayed during the "on" and

"off" states for the UV irradiation at 0 V bias. The UV sensing performance via the NNS/TNAs heterojunctions could be effectively tuned by controlling the NNS layer thickness through the deposition time. The photocurrent measured from the fabricated self-powered UV photosensor was improved with increasing thickness of NNS from 140 to 170 nm under the UV irradiation (365 nm, 750 μWcm^{-2}) at 0 V bias. The increased performance of the photocurrent was due to the increased photogenerated charge carriers for the NNS/TNAs. However, a further increase in the NNS thickness reduced the photocurrent density to some extent. This photocurrent decrease was due to recombination of photo-generated electron-hole pairs, which reduced the total gain of the photocurrent. The best performance of the fabricated UV sensor at 0 V bias was obtained for the TN_3 sample that had a measured photocurrent density of 0.510 $\mu A/cm^2$. In addition, the TN_3 sample also showed the highest sensitivity value of 127.5.

Declaration of Competing Interest

The authors declare that they have no known competing financial interests or personal relationships that could have appeared to influence the work reported in this paper.

Acknowledgements

This work was supported by the ASEAN-India Research & Training Fellowship Scheme (IMRC/AISTDF/R&D/P-1/2017). The authors acknowledge the Ministry of Education Malaysia for the funding of Fundamental Research Grant Scheme (FRGS) (File No: FRGS/1/2018/TK04/UITM/02/23) received for this research. The authors also would like to thank the Institute of Research Management and Innovation (IRMI) of UiTM and the International Islamic University Malaysia (IIUM) for their financial support of this research.

References

[1] P. Bindra, A. Hazra, Selective detection of organic vapors using TiO2 nanotubes based single sensor at room temperature, Sens. Actuat. B 290 (2019) 684–690.
[2] D. Maheswari, P. Venkatachalam, Enhancing the performance of dye-sensitized solar cells based on organic dye sensitized TiO2 nanoparticles/nanowires composite photoanodes with ionic liquid electrolyte, Measurement 60 (2015) 146–154.
[3] A.M. Selman, Z. Hassan, M. Husham, Structural and photoluminescence studies of rutile TiO2 nanorods prepared by chemical bath deposition method on Si substrates at different pH values, Measurement 56 (2014) 155–162.
[4] K.M. Chahrour, F.K. Yam, R. Abdalrheem, High-performance UV photodetector of anodic rutile TiO2 nanotube arrays, Mater. Lett. 248 (2019) 161–164.
[5] X. Kang, S. Liu, Z. Dai, Y. He, X. Song, Z. Tan, Titanium dioxide: from engineering to applications, Catalysts 9 (2019) 191.
[6] C.-J. Chen, C.-H. Liao, K.-C. Hsu, Y.-T. Wu, J.C.S. Wu, P-N junction mechanism on improved NiO/TiO_2 photocatalyst, Catal. Commun. 12 (2011) 1307–1310.
[7] M. Wang, Y. Hu, J. Han, R. Guo, H. Xiong, Y. Yin, TiO2/NiO hybrid shells: p-n junction photocatalysts with enhanced activity under visible light, J. Mater. Chem. A 3 (2015) 20727–20735.
[8] T. Łęcki, K. Zarębska, K. Sobczak, M. Skompska, Photocatalytic degradation of 4-chlorophenol with the use of FTO/TiO2/SrTiO3 composite prepared by microwave-assisted hydrothermal method, Appl. Surf. Sci. 470 (2019) 991–1002.
[9] Z. Lian, P. Xu, W. Wang, D. Zhang, S. Xiao, X. Li, G. Li, C_{60}-decorated CdS/TiO_2 mesoporous architectures with enhanced photostability and photocatalytic activity for H_2 evolution, ACS Appl. Mater. Interfaces 7 (2015) 4533–4540.
[10] S. Bassaki, H. Niazi, F. Golestani-Fard, R. Naghizadeh, R. Bayati, Enhanced photocatalytic activity in p-NiO grafted n-TiO_2 porous coatings, J. Mater. Sci. Technol. 31 (2015) 355–360.
[11] S.A. Rawool, M.R. Pai, A.M. Banerjee, A. Arya, R.S. Ningthoujam, R. Tewari, R. Rao, B. Chalke, P. Ayyub, A.K. Tripathi, S.R. Bharadwaj, pn Heterojunctions in NiO:TiO2 composites with type-II band alignment assisting sunlight driven photocatalytic H2 generation, Appl. Catal. B 221 (2018) 443–458.
[12] M. Enhessari, A. Salehabadi, A. Khoobi, R. Amiri, Kinetic properties and structural analysis of LaCrO 3 nanoparticles, Mater. Sci. Poland 35 (2017) 368–373.
[13] H. Eskandarloo, A. Badiei, M.A. Behnajady, Study of the effect of additives on the photocatalytic degradation of a triphenylmethane dye in the presence of immobilized TiO_2/NiO nanoparticles: artificial neural network modeling, Ind. Eng. Chem. Res. 53 (2014) 6881–6895.
[14] F. Hashemzadeh, A. Gaffarinejad, R. Rahimi, Porous p-NiO/n-Nb_2O_5 nanocomposites prepared by an EISA route with enhanced photocatalytic activity in simultaneous Cr(VI) reduction and methyl orange decolorization under visible light irradiation, J. Hazard. Mater. 286 (2015) 64–74.
[15] C.J. Flynn, S.M. McCullough, E. Oh, L. Li, C.C. Mercado, B.H. Farnum, W. Li, C.L. Donley, W. You, A.J. Nozik, J.R. McBride, T.J. Meyer, Y. Kanai, J.F. Cahoon, Site-selective passivation of defects in NiO solar photocathodes by targeted atomic deposition, ACS Appl. Mater. Interfaces 8 (2016) 4754–4761.
[16] A.M. Ferrari, C. Pisani, F. Cinquini, L. Giordano, G. Pacchioni, Cationic and anionic vacancies on the NiO(100) surface: DFT+U and hybrid functional density functional theory calculations, J. Chem. Phys. 127 (2007) 174711.
[17] C. Feng, Z. Jiang, B. Chen, P. Cheng, Y. Wang, C. Huang, Aluminum-doped NiO nanofibers as chemical sensors for selective and sensitive methanol detection, Anal. Meth. 11 (2019) 575–581.
[18] M.A.R. Abdullah, M.H. Mamat, A.S. Ismail, M.F. Malek, A.B. Suriani, M.K. Ahmad, I.B. Shameem Banu, R. Amiruddin, M. Rusop, Direct and seedless growth of Nickel Oxide nanosheet architectures on ITO using a novel solution immersion method, Mater. Lett. 236 (2019) 460–464.
[19] C.-S. Chou, Y.-J. Lin, R.-Y. Yang, K.-H. Liu, Preparation of TiO_2/NiO composite particles and their applications in dye-sensitized solar cells, Adv. Powder Technol. 22 (2011) 31–42.
[20] Z. Wu, Y. Wang, L. Sun, Y. Mao, M. Wang, C. Lin, An ultrasound-assisted deposition of NiO nanoparticles on TiO_2 nanotube arrays for enhanced photocatalytic activity, J. Mater. Chem. A 2 (2014) 8223–8229.
[21] S. Sumikura, S. Mori, S. Shimizu, H. Usami, E. Suzuki, Syntheses of NiO nanoporous films using nonionic triblock co-polymer templates and their application to photo-cathodes of p-type dye-sensitized solar cells, J. Photochem. Photobiol. A 199 (2008) 1–7.
[22] C. Gao, X. Li, X. Zhu, L. Chen, Y. Wang, F. Teng, Z. Zhang, H. Duan, E. Xie, High performance, self-powered UV-photodetector based on ultrathin, transparent, SnO_2–TiO_2 core–shell electrodes, J. Alloy. Compd. 616 (2014) 510–515.
[23] M. Zhang, D. Li, J. Zhou, W. Chen, S. Ruan, Ultraviolet detector based on TiO_2 nanowire array–polymer hybrids with low dark current, J. Alloy. Compd. 618 (2015) 233–235.
[24] M. Iraj, F.D. Nayeri, E. Asl-Soleimani, K. Narimani, Controlled growth of vertically aligned TiO_2 nanorod arrays using the improved hydrothermal method and their application to dye-sensitized solar cells, J. Alloy. Compd. 659 (2016) 44–50.
[25] M.M. Yusoff, M.H. Mamat, M.F. Malek, A.B. Suriani, A. Mohamed, M.K. Ahmad, S.A.H. Alrokayan, H.A. Khan, M. Rusop, Growth of titanium dioxide nanorod arrays through the aqueous chemical route under a novel and facile low-cost method, Mater. Lett. 164 (2016) 294–298.
[26] M.M. Yusoff, M.H. Mamat, A.S. Ismail, M.F. Malek, Z. Khusaimi, A.B. Suriani, A. Mohamed, M.K. Ahmad, M. Rusop, Enhancing the performance of self-powered ultraviolet photosensor using rapid aqueous chemical-grown aluminum-doped titanium oxide nanorod arrays as electron transport layer, Thin Solid Films 655 (2018) 1–12.
[27] G. Cai, J. Tu, D. Zhou, L. Li, J. Zhang, X. Wang, C. Gu, Constructed TiO_2/NiO core/shell nanorod array for efficient electrochromic application, J. Phys. Chem. C 118 (2014) 6690–6696.
[28] M. Ye, D. Zheng, M. Lv, C. Chen, C. Lin, Z. Lin, Hierarchically structured nanotubes for highly efficient dye-sensitized solar cells, Adv. Mater. 25 (2013) 3039–3044.
[29] M. Zhang, M. Zhang, S. Shi, X. Song, Z. Sun, An approach toward TiO_2 nanostructure growth with tunable properties: influence of reaction time in a hydrothermal process, J. Alloy. Compd. 591 (2014) 213–217.
[30] P. Jain, P. Arun, Influence of grain size on the band-gap of annealed SnS thin films, Thin Solid Films 548 (2013) 241–246.
[31] M. Ben Amor, A. Boukhachem, K. Boubaker, M. Amlouk, Structural optical and electrical studies on Mg-doped NiO thin films for sensitivity applications, Mater. Sci. Semicond. Process. 27 (2014) 994–1006.
[32] P. Ravikumar, B. Kisan, A. Perumal, Thickness dependent ferromagnetism in thermally decomposed NiO thin films, J. Magn. Magn. Mater. 418 (2016) 86–91.
[33] S. Batakrushna, P.K. Giri, I. Kenji, F. Minoru, Microscopic origin of lattice contraction and expansion in undoped rutile TiO_2 nanostructures, J. Phys. D Appl. Phys. 47 (2014) 215302.
[34] M. Landmann, E. Rauls, W.G. Schmidt, The electronic structure and optical response of rutile, anatase and brookite TiO_2, J. Phys.: Condens. Matter 24 (2012) 195503.
[35] J. Zhang, P. Zhou, J. Liu, J. Yu, New understanding of the difference of photocatalytic activity among anatase, rutile and brookite TiO_2, PCCP 16 (2014) 20382–20386.
[36] M.T. Uddin, Y. Nicolas, C. Olivier, W. Jaegermann, N. Rockstroh, H. Junge, T. Toupance, Band alignment investigations of heterostructure NiO/TiO_2 nanomaterials used as efficient heterojunction earth-abundant metal oxide photocatalysts for hydrogen production, PCCP 19 (2017) 19279–19288.
[37] P. Lobotka, P. Kunzo, Polymer/Carbon Composites for Sensing, in: K.K. Kar, J.K. Pandey, S. Rana (Eds.), Handbook of Polymer Nanocomposites. Processing, Performance and Application: Volume B: Carbon Nanotube Based Polymer Composites, Springer, Berlin, Heidelberg, Berlin, Heidelberg, 2015, pp. 577–601.
[38] L.N. Robert Boylestad, Electronic Devices and Circuit Theory, Pearson Education, 2006.

[39] D. Ju, H. Xu, Z. Qiu, J. Guo, J. Zhang, B. Cao, Highly sensitive and selective triethylamine-sensing properties of nanosheets directly grown on ceramic tube by forming NiO/ZnO PN heterojunction, Sens. Actuat. B 200 (2014) 288–296.
[40] A. Mills, S. Le Hunte, An overview of semiconductor photocatalysis, J. Photochem. Photobiol. A 108 (1997) 1–35.
[41] E.H. Rhoderick, R.H. Williams, Metal-Semiconductor Contacts, Clarendon Press, 1988.
[42] Y. Chen, J.C. Crittenden, S. Hackney, L. Sutter, D.W. Hand, Preparation of a novel TiO_2-based p−n junction nanotube photocatalyst, Environ. Sci. Technol. 39 (2005) 1201–1208.
[43] S.R. Jiang, B.X. Feng, P.X. Yan, X.M. Cai, S.Y. Lu, The effect of annealing on the electrochromic properties of microcrystalline NiOx films prepared by reactive magnetron rf sputtering, Appl. Surf. Sci. 174 (2001) 125–131.
[44] J. Bandara, H. Weerasinghe, Solid-state dye-sensitized solar cell with p-type NiO as a hole collector, Sol. Energy Mater. Sol. Cells 85 (2005) 385–390.
[45] C. Cao, C. Hu, X. Wang, S. Wang, Y. Tian, H. Zhang, UV sensor based on TiO2 nanorod arrays on FTO thin film, Sens. Actuat. B 156 (2011) 114–119.
[46] M. Razeghi, A. Rogalski, Semiconductor ultraviolet detectors, J. Appl. Phys. 79 (1996) 7433.
[47] Y.-R. Li, C.-Y. Wan, C.-T. Chang, W.-L. Tsai, Y.-C. Huang, K.-Y. Wang, P.-Y. Yang, H.-C. Cheng, Thickness effect of NiO on the performance of ultraviolet sensors with p-NiO/n-ZnO nanowire heterojunction structure, Vacuum 118 (2015) 48–54.
[48] T. Zhai, L. Li, X. Wang, X. Fang, Y. Bando, D. Golberg, Recent Developments in One-Dimensional Inorganic Nanostructures for Photodetectors, Adv. Funct. Mater. 20 (2010) 4233–4248.
[49] J.D. Prades, F. Hernandez-Ramirez, R. Jimenez-Diaz, M. Manzanares, T. Andreu, A. Cirera, A. Romano-Rodriguez, J.R. Morante, The effects of electron–hole separation on the photoconductivity of individual metal oxide nanowires, Nanotechnology 19 (2008) 465501.
[50] X. Li, C. Gao, H. Duan, B. Lu, X. Pan, E. Xie, Nanocrystalline TiO_2 film based photoelectrochemical cell as self-powered UV-photodetector, Nano Energy 1 (2012) 640–645.
[51] A. Ghasempour Ardakani, M. Pazoki, S.M. Mahdavi, A.R. Bahrampour, N. Taghavinia, Ultraviolet photodetectors based on ZnO sheets: the effect of sheet size on photoresponse properties, Appl. Surf. Sci. 258 (2012) 5405–5411.
[52] Z. Alaie, S. Mohammad Nejad, M.H. Yousefi, Recent advances in ultraviolet photodetectors, Mater. Sci. Semicond. Process. 29 (2015) 16–55.
[53] T. Srivastava, G. Bajpai, G. Rathore, S.W. Liu, S. Biring, S. Sen, Vanadium substitution: a simple and economic way to improve UV sensing in ZnO, J. Appl. Phys. 123 (2018) 161407.
[54] A.S. Ismail, M.H. Mamat, I.B. Shameem Banu, R. Amiruddin, M.F. Malek, N. Parimon, A.S. Zoolfakar, N.D. Md. Sin, A.B. Suriani, M.K. Ahmad, M. Rusop, Structural modification of ZnO nanorod array through Fe-doping: ramification on UV and humidity sensing properties, Nano Struct. Nano-Objects 18 (2019) 100262.
[55] L. Zhang, E. Reisner, J.J. Baumberg, Al-doped ZnO inverse opal networks as efficient electron collectors in $BiVO_4$ photoanodes for solar water oxidation, Energy Environ. Sci. 7 (2014) 1402–1408.